Structural, morphological and optical properties of cobalt-substituted MgMoO4 ceramics prepared by pyrolysis of citric acid precursors

Hind Lakhlifi, Youssef El Jabbar, Rachida El Ouatib, Lahcen Er-Rakho, Sophie Guillemet-Fritsch, Bernard Durand

Structural, morphological and optical properties of cobalt-substituted $MgMoO_4$ ceramics prepared by pyrolysis of citric acid precursors

Hind Lakhlifi[a,*], Youssef El Jabbar[a], Rachida El Ouatib[a], Lahcen Er-Rakho[a], Sophie Guillemet-Fritsch[b], Bernard Durand[b]

[a] *Laboratoire de Physico-chimie des Matériaux Inorganiques, Faculté des sciences Aïn chock, Université Hassan II, Bb. 5366 Mâarif, Casablanca, Morocco*
[b] *Institut Carnot CIRIMAT, CNRS Université de Toulouse, 118 route de Narbonne, 31062 Toulouse Cedex 9, France.*

ARTICLE INFO

Keywords:
Magnesium-cobalt molybdate
Sol-gel
pigment
specific surface area
SEM analysis

ABSTRACT

Magnesium-cobalt molybdate composites ($Mg_{1-x}Co_xMoO_4$: $x = 0$, 0.3, 0.4, 0.6, 0.8 and 1) were successfully synthesized through a facile sol-gel synthesis at low temperature, and characterized by thermogravimetric and differential thermal analysis (TG-DTA), X-ray diffraction (XRD), Fourier transform-infrared spectroscopy (FTIR), Raman spectroscopy, scanning electron microscopy (SEM), UV-Vis spectroscopy and colorimetric measurements using the CIE L*a*b* colour system. The surface specific area was calculated using the Brunauer–Emmett–Teller analysis in the adsorption/desorption isotherm. The examination of the X-ray diffractograms of the unground milled solid solutions of $Mg_{1-x}Co_xMoO_4$ ($0 \leq x \leq 1$) presented a single continuous system related to monoclinic β-$MgMoO_4$. The absorbance spectra of the $Mg_{1-x}Co_xMoO_4$ pigments confirmed the insertion of cobalt in the β-$MgMoO_4$ matrix. The CIE-L*a*b* colour coordinates indicated that the intense purple colour was obtained for $x = 0.6$.

1. Introduction

Nanomaterials have been widely studied in recent years. Their properties vary according to their chemical compositions, sizes, and specific surface areas. These materials of the future have the potential to save energy while protecting the environment; however, achieving these objectives requires excellent mastery of nanomaterial production processes, which must be low cost from an energy point of view [1,2]. Molybdates, which also have interesting physical properties [3], are widely used in various industrial sectors. Metal molybdates of monoclinic structures have many potential applications involving, for example, photoluminescence, semiconductor lasers, magnets, lithium-ion batteries, microwaves, catalysts, and photoelectric devices [4–10].

Magnesium-Cobalt Molybdate ($Mg_{1-x}Co_xMoO_4$) is an important technological material used as a catalyst in many chemical and petrochemical processes such as cracking, dehydrogenation, hydrogenation and hydrodesulfurization (HDS). These molybdates also exhibit interesting optical, catalytic and dielectric properties. They have been used as pigments for decades and in particular as an analytical dosing agent.

The solid-solid method is often used for the synthesis of $Mg_{1-x}Co_xMoO_4$ molybdates. This process requires heat treatment at high temperatures, and typically results in powders of poor chemical and morphological homogeneity [11]. The objective of this work is to develop $Mg_{1-x}Co_xMoO_4$ ($0 \leq x \leq 1$) molybdates of nanometric size at low temperatures by pyrolysis of citrate precursors. Extremely pure multi-component oxides of submicron grain size and high chemical homogeneity can be obtained rapidly and easily by producing polymerizable complexes [12]. Typically, for molybdates of the formula $A^{2+}MoO_4$ ($A^{2+} = Mg^{2+}$, Co^{2+}…) and of the monoclinic type in the space group C2/m in the polymorph α, all the cations are in octahedral coordination. In the β phase, the divalent cation remains in the octahedral site, while the coordination of Mo evolves toward a tetrahedral site [13,14]. The products thus obtained adopt the α or β type molybdates of divalent 3d element monoclinics depending only on whether they are cooled to ambient temperature with or without grinding. Mg^{2+} ions have a strong preference for regular octahedral environments in the β phase rather than the α phase [15,16]. When Mg is substituted for Co, the likelihood of affecting the second neighboring Mo atoms increases rapidly, as one Mg atom is surrounded by six Mo atoms [17].

2. Methods and materials

The following reagents were used to develop the precursors of the

* Corresponding author.
E-mail address: lakhlifihind21@gmail.com (H. Lakhlifi).

https://doi.org/10.1016/j.surfin.2020.100718

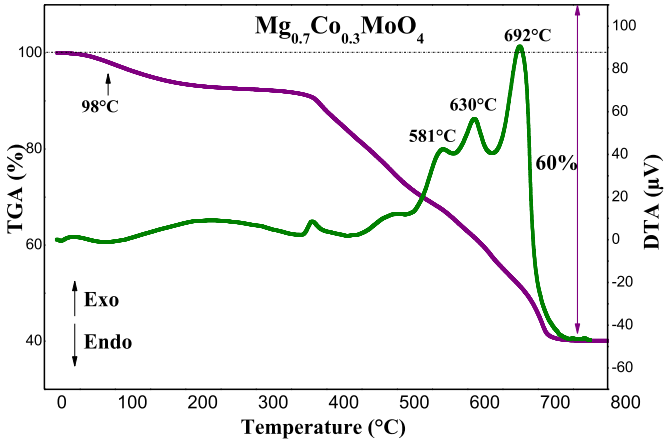

Fig. 1. TG–DTA curves of the $Mg_{0.7}Co_{0.3}MoO_4$ precursor obtained by pyrolysis of citrate precursors.

$Mg_{1-x}Co_xMoO_4$ molybdates: 0.2M magnesium nitrate ($Mg(NO_3)_2{\cdot}6H_2O$) (Aldrich, 98%), 0.2M cobalt nitrate ($Co(NO_3)_2{\cdot}6H_2O$) (Aldrich, 98%),0.2M ammonium heptamolybdate ($(NH_4)_6Mo_7O_{24}.4H_2O$) (Acros, 99%), and citric acid (Acros, 98%). The citric acid makes it possible to complex the metals along the polymer chains. These reagents were mixed in stoichiometric proportions. After evaporation, the precursors obtained were pre-burned at 300°C for 12 hours under air. The resulting black powders were crushed and then maintained at 700°C for 2 hours. Depending on the rate of cobalt added, powders of different colours were obtained after grinding. The resulting powders were characterized using an x-ray diffractometer (Bruker D8 Advance equipped with a LynxEye detector. The X-ray generator (40 kV, 40 mA) is a copper anticathode tube that uses the CuKα line. A graphite monochromator eliminates the Kβ lines. The wavelength of the Kα1 / Kα2 lines of copper is 0.15406 / 0.15443 nm. The phases obtained are analyzed using Eva PLUS software by comparing the positions and intensities of the different diffraction lines observed with those available in the PDF-4-2010 Database established by the ICDD (International Center for Diffraction Data). The infrared spectra were taken using a Fourier-transform infrared spectrometer (IR Affinity-1S Shimadzu). The Raman spectra were recorded with a LabRAM HR 800 (Horiba Jobin-Yvon) spectrometer. The morphologies of the powders were examined using scanning electronic microscopy (JEOL JSM 6400), and the specific surface areas were determined using the Brunauer–Emmett–Teller (BET) method (Micrometrics Flowsorb II 2300). The colour parameters (L*a*b*) were measured using the CIE Lab system colorimeter (CR-400/410, KONICA MINOLTA).

3. Results and discussion

3.1. Thermal decomposition (TG-DTA)

The decomposition of the organic part of the xerogels is an essential parameter to be defined in order to optimize the future heat treatments necessary for the preparation of the powders. The thermogravimetric analysis curve of the magnesium-based $Mg_{0.7}Co_{0.3}MoO_4$ (x = 0.3)

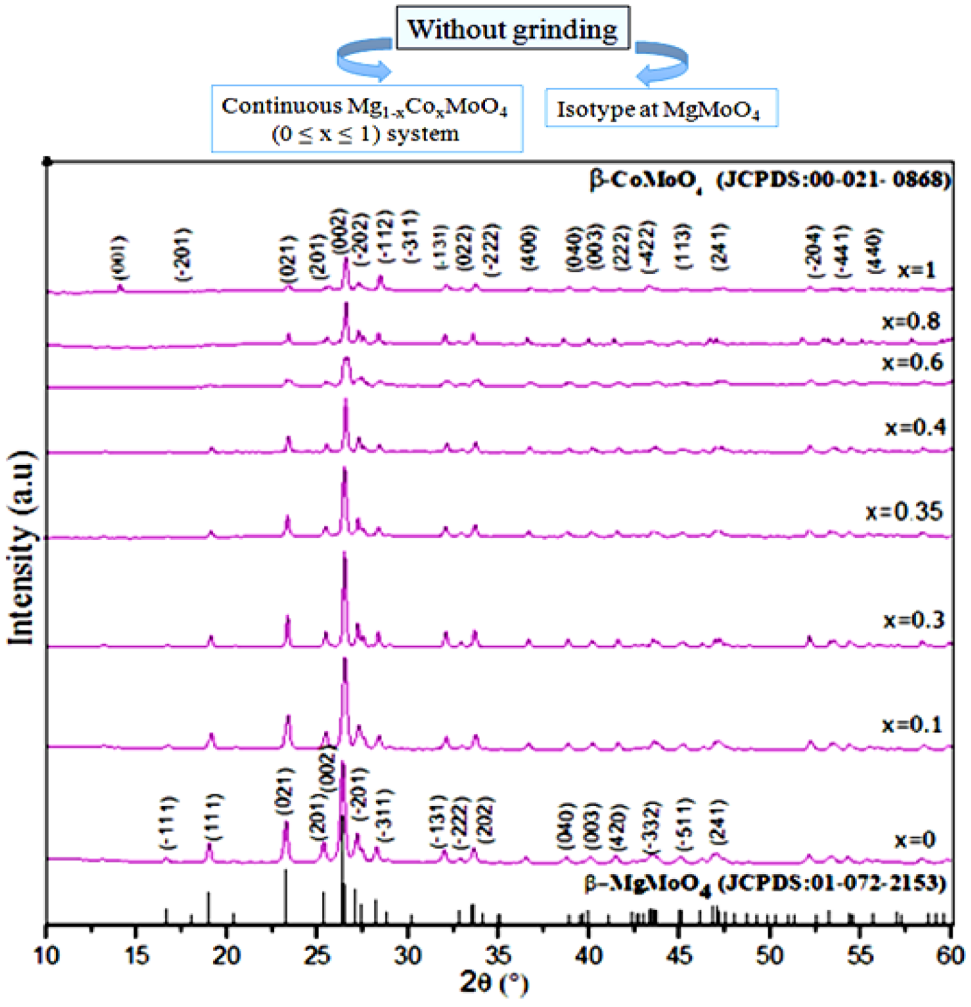

Fig. 2. XRD patterns of $Mg_{1-x}Co_xMoO_4 (0 \leq x \leq 1)$ compounds prepared by sol gel route without grinding

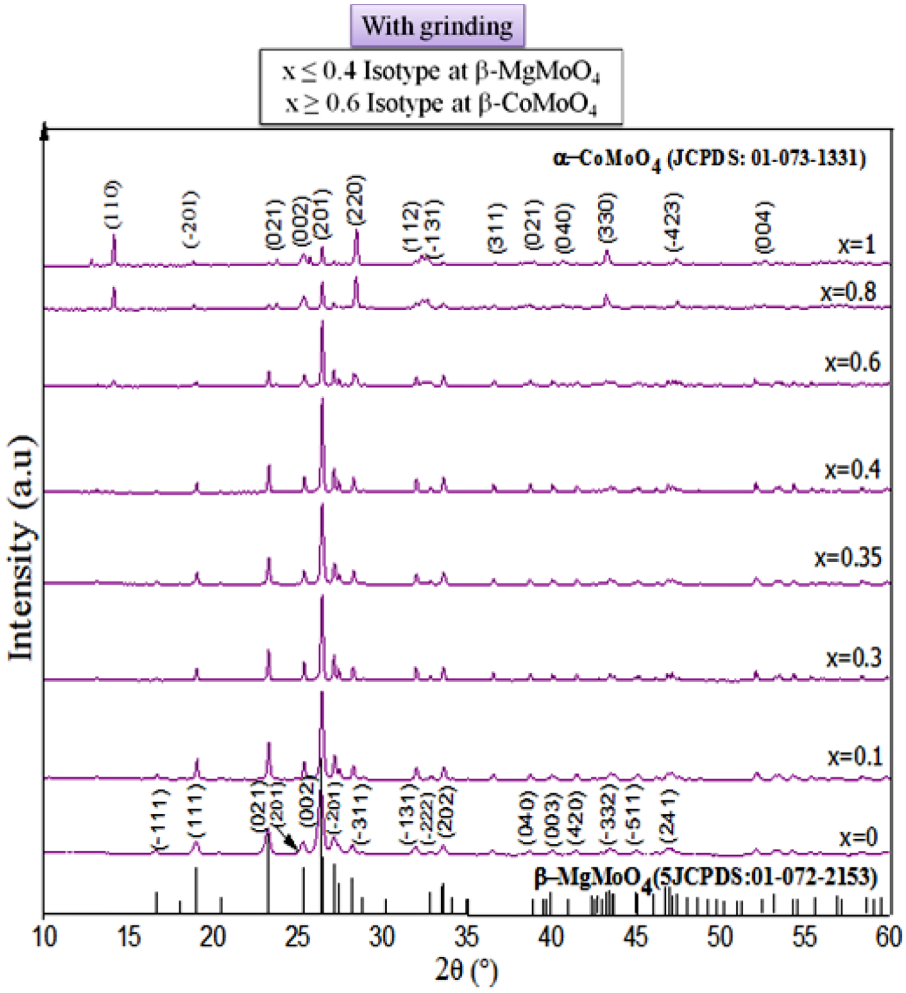

Fig. 3. XRD patterns of $Mg_{1-x}Co_xMoO_4$ ($0 \leq x \leq 1$) compounds prepared by sol gel route with grinding.

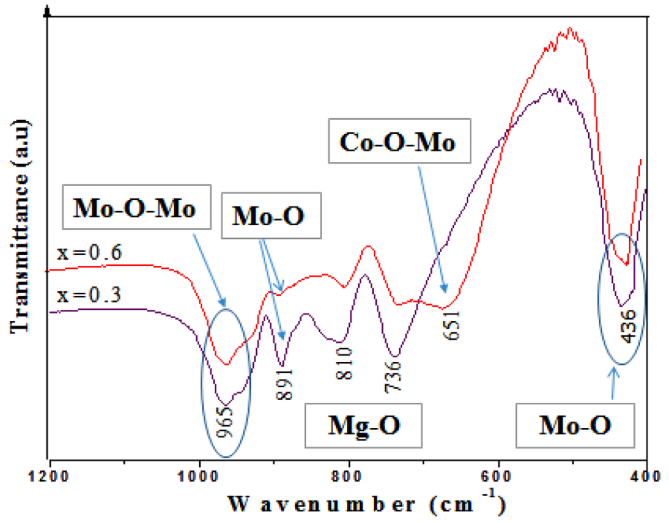

Fig. 4. FT-IR spectra of $Mg_{1-x}Co_xMoO_4$ (x = 0.3 and x = 0.6) powders obtained at 700°C.

precursor in air shows that thermal decomposition occurs in several stages. As shown in Fig. 1, this decomposition starts at approximately 20°C and ends before 700°C. The total weight loss is about 60%. The first weight loss of the molybdate (about 8%) is observed at approximately 98°C; it corresponds to the elimination of water adsorbed on the surfaces of the powders. The second series of successive weight losses observed between 350 and 550°C corresponds to a loss of 24%, and can be attributed to the combustion of the precursor. A final weight loss of 28% is associated with three exothermic peaks located at 581, 630 and 692 °C. This process most likely corresponds to the oxidation of the carbon produced during the combustion of the precursor. No phenomenon is observed above 700°C. This temperature was thus used for the rest of our syntheses.

3.2. X-ray diffraction (XRD)

In order to check the purity of the phases, X-ray diffraction analyses were carried out. The examination of the X-ray diffractograms of the solid solutions of $Mg_{1-x}Co_xMoO_4$ ($0 \leq x \leq 1$) present a single continuous system for the compositions corresponding to $0 \leq x \leq 1$ without grinding and have a single-phase domain related to monoclinic β-$MgMoO_4$ (JCPDS card No. 072-2153) (Fig. 2). For cobalt contents $x \geq 0.6$ in the case of ground powders, the only phase observed is α-$CoMoO_4$ (JCPDS card No. 073-1331) (Fig. 3).

A simple grinding of the powder ($0.6 \leq x \leq 1$), which is purple in color and which corresponds to the allotropic variety β-$CoMoO_4$, leads to powders of green color isotype of the allotropic variety α-$CoMoO_4$ pure. The change in color under the effect of grinding or pressure in general is called the phenomenon of piezochromism. The molybdates isotype of β$CoMoO_4$ are known as piezosensitive (sensitive to grinding) compounds. The grinding of the powders obtained ($Mg_{1-x}Co_xMoO_4$ ($0 \leq x \leq 1$)) was carried out manually with an agate mortar for 5 to 10

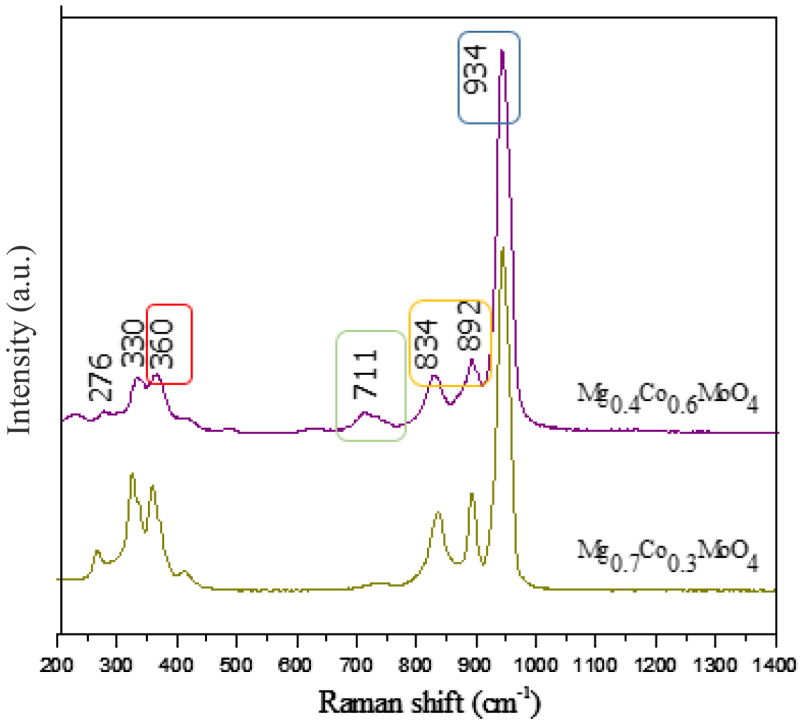

Fig. 5. Raman spectra of the $Mg_{1-x}Co_xMoO_4$ (x = 0.3, 0.6) powders obtained at 700°C.

Table 1
Raman bands, modes and attributions of the $Mg_{1-x}Co_xMoO_4$ ($x=0.3$ and $x=0.6$).

Frequencies (cm_{-1})	Mode and Attribution
934	υ_1(Ag/C_2h) MoO_4: Symmetrical stretch
892-834	υ_3 (Ag/C_2h and Eg/(e.g)) Mo–O–Mo: Ant-isymmetric stretch
711	υ_4 (Bg/D_2h) O-Mo-O: Anti-symmetric oxygen stretching vibration
360	υ_4 (Bg/D_2h): anti-symmetric vibration
330	υ_2(Ag/C_2h): Bending modes
276	Free rotation mode

Table 2
Elementary grain size solid solutions $Mg_{1-x}Co_xMoO_4$ ($x = 0.3$ and $x = 0.6$).

Synthesis route	The Co^{2+} amount incorporated (x)	Specific surface area BET (m^2/g)	Average particle size BET (nm)
Sol- gel (700°C)	0.3	0.41	3622
	0.6	0.77	1824

min (Fig. 3):

- For the compositions $0 \leq x \leq 0.4$, an iso-type monoclinic phase of β-$MgMoO_4$ is observed.
- For cobalt contents $0.6 \leq x \leq 1$, the only phase observed is α-$CoMoO_4$ with a green color, it is a transition phenomenon of β ——> α.

These results are in good agreement to those obtained by solid-state reaction [18].

3.3. Infrared spectroscopy (FT-IR)

Spectroscopy analyses (FTIR) were carried out on the $Mg_{1-x}Co_xMoO_4$ ($x=0.3$ and $x=0.6$) powders prepared by sol gel route and treated at 700°C (Fig. 4). Infrared spectra show the presence of the Mo-O-Mo stretching vibration bands observed at 950 and 911 cm^{-1} [19,20].The band located at 856 cm^{-1} is associated with the vibration mode of the Mo-O band [21]. Thus, the bands observed at 744 and 710 cm^{-1} are associated with the vibration of the Mg-O band [22], the band at 495 cm^{-1} is specific to the vibrations of the Co-O-Mo band [23]. While the peak located at 436 cm^{-1} is due to the bending mode of Mo–O [24].

3.4. Raman spectroscopy

In order to confirm the results obtained previously, analyses using Raman spectroscopy were carried out on the $Mg_{1-x}Co_xMoO_4$ powders (x = 0.3 and x = 0.6) produced by sol–gel route (Fig. 5). Generally, Raman bands corresponding to the symmetrical stretching (υ_1) and asymmetrical stretching (υ_3) modes were observed in the 700-1000 cm^{-1} region, whereas those corresponding to the symmetrical modes (υ_2) and asymmetrical modes (υ_4) were observed in the 50-520 cm^{-1} region [25]. With regards to the solid solutions of $Mg_{1-x}Co_xMoO_4$ (x = 0.3 and x = 0.6) prepared through the sol–gel route, the most intense vibration observed at 934 cm^{-1} is assigned to the mode d symmetric stretch υ_1(Ag) of the MoO_4^{2-}tetrahedron [26] of the C_{2h} point group. Those located at 892 and 834 cm^{-1} correspond to the anti-symmetric stretching υ3 (Bg/D_2h) and υ3 (Eg) vibration modes of the Mo–O–Mo of German entartet (e.g.), respectively [21]; the band observed at 711 cm^{-1} corresponds to the antisymmetric stretching modes of oxygen in the O-Mo-O band [27]; The peaks at 360 and 330 cm^{-1} correspond to the anti-symmetric υ_4(Bg/D_2h) and υ_2(Ag/C_2h) bending modes, respectively [28–31]. Thus, the free rotation mode was observed at 276 cm^{-1} [32]. These results were consistent with those obtained by diffraction analysis techniques X-rays and infrared spectroscopy (FTIR). The Raman bands of the compositions x = 0.3 and x = 0.6 are summarised in Table 1.

3.5. Specific surface area measurements (BET)

Specific surface area measurements were carried out on the

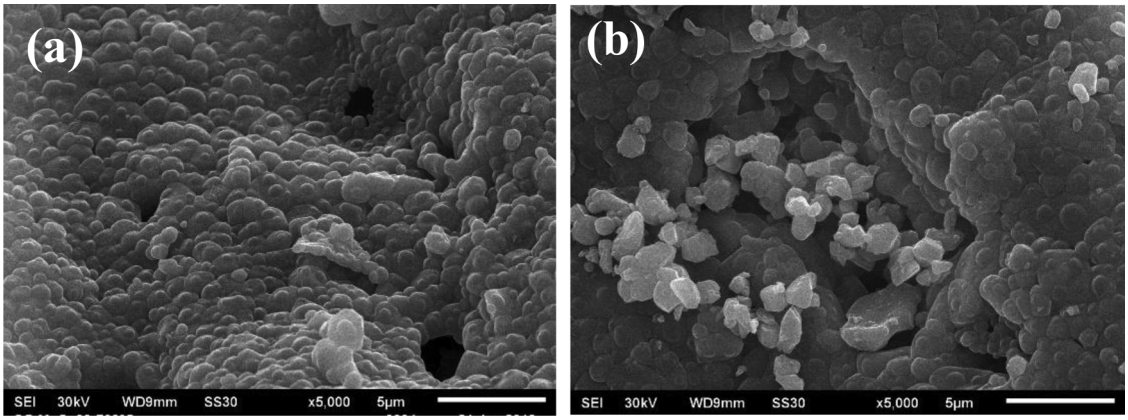

Fig. 6. SEM micrographs of $Mg_{1-x}Co_xMoO_4$ powders (a): x = 0.3 and (b): x = 0.6 prepared by sol-gel route.

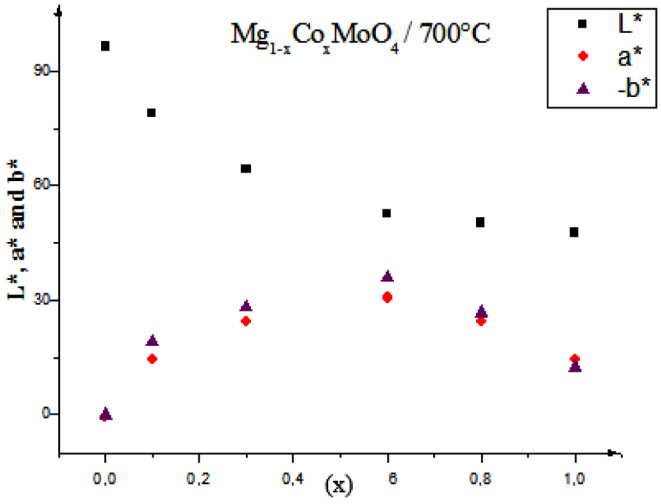

Fig. 7. Evolution of the colour parameters of $Mg_{1-x}Co_xMoO_4$ ($0 \leq x \leq 1$) powders obtained by sol-gel route.

$Mg_{1-x}Co_xMoO_4$ (x = 0.3, 0.6) powdered samples. Table 2 presents these measurements and the average sizes of the particles which were calculated, taking into consideration that the particles are spherical and individualised. It should be noted that the powders obtained via the sol–gel route have low specific surfaces that vary from 0.4 to 0.8 m^2/g which depending on the rate of incorporation of the cobalt.

3.6. Scanning electron microscopy (SEM)

The SEM micrographs for $Mg_{1-x}Co_xMoO_4$ ($x = 0.3$ and $x = 0.6$) prepared at 700°C via sol-gel route show a powders formed by compact porous agglomerates forming cages (Fig. 6a and b).The porosity comes from the rapid dissipation of the gaseous products (NO_2, CO_2 and H_2O) formed during the combustion. The particles forming the agglomerates range in size from 1 to 5 μm). These images show advanced sintering, which confirms the low values of the specific BET surfaces obtained.

3.7. Colorimetric measurements (CIE L*a*b*)

The colorimetric parameters (L* a* b*) of the $Mg_{1-x}Co_xMoO_4$ powders for the compositions $0 \leq x \leq 1$ obtained at 700°C through the

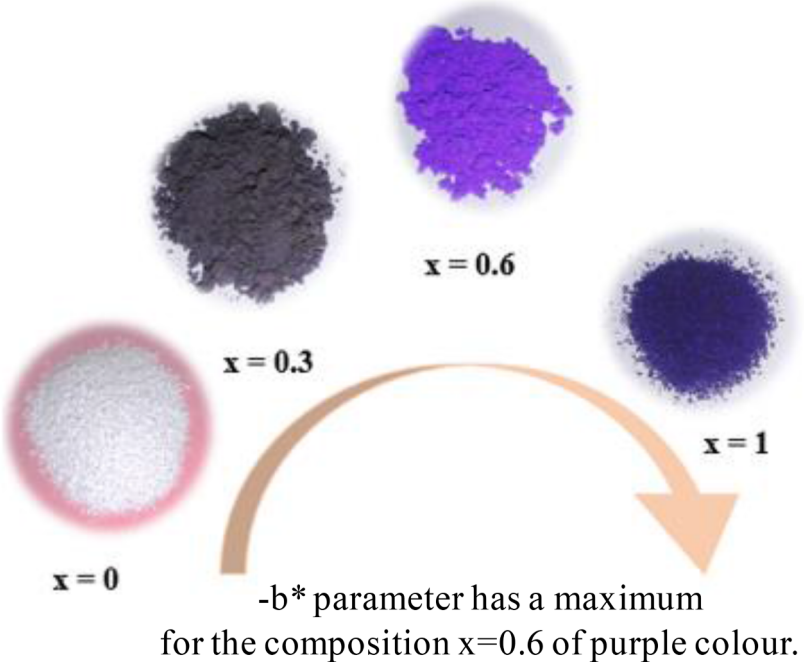

Fig. 8. Shades of colours of $Mg_{1-x}Co_xMoO_4$ (x = 0, 0.3, 0.6, 1) powders obtained at 700°C without grinding.

sol–gel method were measured in the CIE L*a*b* system (Fig. 7). We noted a maximum value for the composition $x = 0.6$ with purple colour. Fig. 8 shows the different shades of purple obtained essentially depend on the content of cobalt x, such that $0 \leq x \leq 1$.

4. Conclusion

Cobalt-substituted $MgMoO_4$ compounds were prepared through the sol-gel route. The X-ray diffraction result shows the formation of continuous systems of the solid solution $Mg_{1-x}Co_xMoO_4$ ($0 \leq x \leq 1$) and the grinding of these powders seems to have an influence on the phase obtained. In fact, for the compositions $0 \leq x \leq 1$:

- Without grinding, they present a single-phase domain of monoclinic symmetry isotype at β-$MgMoO_4$.
- With grinding, the fractions $x \geq 0.6$ show, a single-phase isotype with α-$CoMoO_4$.

The ceramic pigments obtained have an advanced pre-sintering state, which explains the low values of specific surface area between 0.41 and 0.77 m^2/g. The measurements of the L*a*b* colorimetric coordinates show that the component (–b*), which is characterised by purple colour, has a maximum value in the case of $Mg_{0.4}Co_{0.6}MoO_4$.

CRediT authorship contribution statement

Hind Lakhlifi: Conceptualization, Software, Formal analysis, Writing - original draft. **Youssef El Jabbar:** Conceptualization, Software, Formal analysis, Conceptualization, Software, Formal analysis. **Rachida El Ouatib:** Supervision, Project administration, Validation. **Lahcen Er-Rakho:** Methodology, Data curation. **Sophie Guillemet-Fritsch:** Resources, Visualization. **Bernard Durand:** Investigation, Visualization, Supervision.

Declaration of Competing Interest

The authors declare that they have no known competing financial interests or personal relationships that could have appeared to influence the work reported in this paper.

References

[1] K. Li, R. Van Deun, Photoluminescence and energy transfer properties of a novel molybdate $KBaY(MoO_4)_3$: Ln^{3+} (Ln^{3+} = Tb^{3+}, Eu^{3+}, Sm^{3+}, Tb^{3+}/Eu^{3+}, Tb^{3+}/Sm^{3+}) as a multi-color emitting phosphor for UV w-LEDs, Dalton Trans 47 (2018) 6995–7004, https://doi.org/10.1039/C8DT01011K.

[2] D.B. Panemangalore, R. Shabadi, M. Gupta, G. Ji, Effect of fluoride coatings on the corrosion behavior of Mg–Zn–Er alloys, Surf. Interfaces. 14 (2019) 72–81, https://doi.org/10.1016/j.surfin.2018.11.007.

[3] R.S. Mohar, I. Sugihartono, V. Fauzia, A.A. Umar, Dependence of optical properties of Mg-doped ZnO nanorods on Al dopant, Surf. Interfaces. 19 (2020) 100518, , https://doi.org/10.1016/j.surfin.2020.100518.

[4] M. Shkir, Z.R. Khan, M.S. Hamdy, H. Algarni, S. AlFaify, A facile microwave-assisted synthesis of $PbMoO_4$ nanoparticles and their key characteristics analysis: a goodcontender for photocatalytic applications, Mater. Res. Express. 5 (2018) 095032, , https://doi.org/10.1088/2053-1591/aad893.

[5] R. Karthik, J. Vinoth Kumar, S.-M. Chen, C. Karuppiah, Y.-H. Cheng, V. Muthuraj, A Study of Electrocatalytic and Photocatalytic Activity of Cerium Molybdate Nanocubes Decorated Graphene Oxide for the Sensing and Degradation of Antibiotic Drug Chloramphenicol, ACS Appl. Mater. Interfaces. 9 (2017) 6547–6559, https://doi.org/10.1021/acsami.6b14242.

[6] A.J. Howarth, T.C. Wang, S.S. Al-Juaid, S.G. Aziz, J.T. Hupp, O.K. Farha, Efficient extraction of sulfate from water using a Zr-metal–organic framework, Dalton Trans 45 (2016) 93–97, https://doi.org/10.1039/C5DT04163E.

[7] B. Tawiah, C. Narh, M. Li, L. Zhang, S. Fu, Polymer-Encapsulated Colorful Al Pigments with High NIR and UV Reflectance and Their Application in Textiles, Ind. Eng. Chem. Res. 54 (2015) 11858–11865, https://doi.org/10.1021/acs.iecr.5b03555.

[8] C. Agustín-Sáenz, E. Martín-Ugarte, J.B. Jorcin, G. Imbuluzqueta, P. Santa Coloma, U. Izagirre-Etxeberria, Effect of organic precursor in hybrid sol–gel coatings for corrosion protection and the application on hot dip galvanised steel, J. Sol-Gel Sci. Technol. 89 (2019) 264–283, https://doi.org/10.1007/s10971-018-4840-6.

[9] H. Li, Q. Yang, F. Mo, G. Liang, Z. Liu, Z. Tang, L. Ma, J. Liu, Z. Shi, C. Zhi, MoS_2 nanosheets with expanded interlayer spacing for rechargeable aqueous Zn-ion batteries, Energy Storage Mater 19 (2019) 94–101, https://doi.org/10.1016/j.ensm.2018.10.005.

[10] H. Ou, S. Xu, Z. Xiao, H. Fu, Y. Luo, Preparation and Photoelectric Properties of MoSMicrospheres, IOP Conf. Ser. Mater. Sci. Eng. 493 (2019) 012072, , https://doi.org/10.1088/1757-899X/493/1/012072.

[11] L. Cornu, V. Jubera, A. Demourgues, G. Salek, M. Gaudon, Luminescence properties and pigment properties of A-doped (Zn,Mg)MoO_4 triclinic oxides (with A = Co, Ni, Cu or Mn), Ceram. Int. 43 (2017) 13377–13387, https://doi.org/10.1016/j.ceramint.2017.07.040.

[12] V. Claude, J.G. Mahy, T. Lohay, R.G. Tilkin, F. Micheli, S.D. Lambert, Sol–gel synthesis of Ni/Al_2O_3 catalysts for toluene reforming: Support modification with alkali, alkaline earth or rare-earth dopant (Ca, K, Mg or Ce), Surf. Interfaces. 20 (2020) 100511, , https://doi.org/10.1016/j.surfin.2020.100511.

[13] Y. Zhao, X. He, R. Chen, Q. Liu, J. Liu, J. Yu, J. Li, H. Zhang, H. Dong, M. Zhang, J. Wang, A flexible all-solid-state asymmetric supercapacitors based on hierarchical carbon cloth@$CoMoO_4$@NiCo layered double hydroxide core-shell heterostructures, Chem. Eng. J. 352 (2018) 29–38, https://doi.org/10.1016/j.cej.2018.06.181.

[14] H. Lakhlifi, M. Benchikhi, R.E. Ouatib, L. Er-Rakho, S. Guillemet-Fritsch, B. Durand, Synthesis and physicochemical characterization of pigments based on molybdenum « ZnO-MoO3: Co2+», (2015) 6.

[15] D. Zagorac, J.C. Schön, M. Rosić, J. Zagorac, D. Jordanov, J. Luković, B. Matović, Theoretical and Experimental Study of Structural Phases in $CoMoO_4$, Cryst. Res.Technol. 52 (2017) 1700069, , https://doi.org/10.1002/crat.201700069.

[16] W. Ran, L. Wang, M. Yang, X. Kong, D. Qu, J. Shi, Enhanced energy transfer from Bi^{3+} to Eu^{3+} ions relying on the criss-cross cluster structure in $MgMoO_4$ phosphor, J. Lumin. 192 (2017) 141–147, https://doi.org/10.1016/j.jlumin.2017.06.039.

[17] G.L. Jadhav, S.D. More, C.M. Kale, K.M. Jadhav, Effect of magnesium substitution on the structural, morphological, optical and wettability properties of cobalt ferrite thin films, Phys. B Condens. Matter. 555 (2019) 61–68, https://doi.org/10.1016/j.physb.2018.11.052.

[18] L. Robertson, M. Duttine, M. Gaudon, A. Demourgues, Chemistry of Materials. 23 (2011) 2419–2427, https://doi.org/10.1021/cm200795p.

[19] A. Mobeen Amanulla, Sk.Jasmine Shahina, R. Sundaram, C. Maria Magdalane, K. Kaviyarasu, D. Letsholathebe, S.B. Mohamed, J. Kennedy, M. Maaza, magnetic Antibacterial, optical and humidity sensor studies of β-$CoMoO_4$-Co_3O_4 nanocomposites and its synthesis and characterization, J. Photochem. Photobiol. B. 183 (2018) 233–241, https://doi.org/10.1016/j.jphotobiol.2018.04.034.

[20] H. Lakhlifi, Y. El Jabbar, R. El Ouatib, L. Er-Rakho, B. Durand, S. Guillemet-Fritsch, Synthesis of molybdates $Zn_{1-x}Co_xMoO_4$ ($0 \leq x \leq 1$), by decomposition of the precursors developed by the glycine-nitrate process (GNP), and their characterization, Mater. Sci. Semicond. Process. 114 (2020) 105054, , https://doi.org/10.1016/j.mssp.2020.105054.

[21] A. Uchagawkar, A. Ramanathan, Y. Hu, B. Subramaniam, Highly dispersed molybdenum containing mesoporous silicate (Mo-TUD-1) for olefin metathesis, Catal. Today. 343 (2020) 215–225, https://doi.org/10.1016/j.cattod.2019.03.073.

[22] A.A. Aboul-Enein, A.E. Awadallah, Impact of Co/Mo ratio on the activity of CoMo/MgO catalyst for production of high-quality multi-walled carbon nanotubes from polyethylene waste, Mater. Chem. Phys. 238 (2019) 121879, , https://doi.org/10.1016/j.matchemphys.2019.121879.

[23] V. Jeseentharani, A. Dayalan, K.S. Nagaraja, Co-precipitation synthesis, humidity sensing and photoluminescence properties of nanocrystalline Co^{2+} substituted zinc (II) molybdate ($Zn_{1-x}Co_xMoO_4$; x = 0, 0.3, 0.5, 0.7, 1), Solid State Sci. 67 (2017) 46–58, https://doi.org/10.1016/j.solidstatesciences.2017.02.008.

[24] Ateyya A. Aboul-Enein, Ahmed E. Awadallah, Impact of Co/Mo ratio on the activity of CoMo/MgO catalyst for production of high-quality multi-walled carbon nanotubes from polyethylene waste, J. Materials Chemistry and Physics 238 (2019) 121879, , https://doi.org/10.1016/j.matchemphys.2019.121879.

[25] P.J. Mafa, B. Ntsendwana, B.B. Mamba, A.T. Kuvarega, Visible Light Driven $ZnMoO_4$ /$BiFeWO_6$/rGO Z-Scheme Photocatalyst for the Degradation of Anthraquinonic Dye, J. Phys. Chem. C. 123 (2019) 20605–20616, https://doi.org/10.1021/acs.jpcc.9b05008.

[26] L. Jiang, Z. Wang, H. Chen, Y. Chen, P. Chen, Z. Xu, Thermal annealing effects on the luminescence and scintillation properties of CaMoO4 single crystal grown by Bridgman method, J. Alloys Compd. 734 (2018) 179–187, https://doi.org/10.1016/j.jallcom.2017.11.005.

[27] M. Rodriguez, M.C.P. Stolzemburg, C.G.O. Bruziquesi, A.C. Silva, C.G. Abreu, K.P.F. Siqueira, L.C.A. Oliveira, M.S. Pires, L.C.T. Lacerda, T.C. Ramalho, A. Dias, M.C. Pereira, Electrocatalytic performance of different cobalt molybdate structures for water oxidation in alkaline media, CrystEngComm 20 (2018) 5592–5601, https://doi.org/10.1039/C8CE01073K.

[28] T. Meng, H. Jia, H. Ye, T. Zeng, X. Yang, H. Wang, Y. Zhang, Facile preparation of $CoMoO_4$ nanorods at macroporous carbon hybrid electrocatalyst for non-enzymatic glucose detection, J, Colloid Interface Sci 560 (2020) 1–10, https://doi.org/10.1016/j.jcis.2019.10.054.

[29] Z. Liu, J. Wang, C. Zhan, J. Yu, Y. Cao, J. Tu, C. Shi, Phosphide-oxide honeycomb-like heterostructure CoP@$CoMoO_4$/CC for enhanced hydrogen evolution reaction in alkaline solution, J. Mater. Sci. Technol. 46 (2020) 177–184, https://doi.org/10.1016/j.jmst.2019.12.013.

[30] N. Padmanathan, K.M. Razeeb, S. Selladurai, Hydrothermal synthesis of carbon- and reduced graphene oxide-supported $CoMoO_4$ nanorods for supercapacitor, Ionics 20 (2014) 1323–1334, https://doi.org/10.1007/s11581-014-1089-0.

[31] T. Yang, H. Zhang, Y. luo, L. Mei, D. Guo, Q. Li, T. Wang, Enhanced electrochemical performance of $CoMoO_4$ nanorods/reduced graphene oxide as anode material for lithium ion batteries, Electrochimica Acta 158 (2015) 327–332, https://doi.org/10.1016/j.electacta.2015.01.154.

[32] C. Luz-Lima, J.C. Batista, P.T.C. Freire, G.P. de Sousa, F.E.P. dos Santos, J. Mendes Filho, B.C. Viana, G.D. Saraiva, Temperature-dependent Raman spectroscopy studies of phase transformations in the K_2WO_4 and the $MgMoO_4$ crystals, Vib. Spectrosc. 65 (2013) 58–65, https://doi.org/10.1016/j.vibspec.2012.11.016.